Large-eddy simulations of leading edge film cooling: Analysis of flow structures, effectiveness, and heat transfer coefficient

Ali Rozati, Danesh K. Tafti *

Mechanical Engineering Department, Virginia Polytechnic Institute and State University, 114-I Randolph Hall, Mail code 0238, Blacksburg, VA 24061, USA

Abstract

A numerical investigation is conducted to study leading edge film cooling with large eddy simulation (LES). The domain geometry is adopted from an experimental setup of [Ekkad, S.V., Han, J.C., Du, H., 1998. Detailed film cooling measurement on a cylindrical leading edge model: Effect of free-stream turbulence and coolant density. Journal of Turbomachinery 120, 799–807.] where turbine blade leading edge is represented by a semi-cylindrical blunt body with compound angle of injection. At blowing ratio of 0.4 and coolant to mainstream density ratio of unity, a laminar constant velocity and fully-turbulent coolant jet are studied. In both cases, the results show the existence of an asymmetric counter-rotating vortex pair in the immediate wake of the coolant jet. In addition to these primary structures, vortex tubes on the windward side of the jet are convected downstream over and to the aft- and fore-side of the counter-rotating vortex pair. All these structures play a role in the mixing of mainstream fluid with the coolant. The fully-turbulent coolant jet increases mixing with the mainstream in the outer shear layer but does not directly influence the flow dynamics in the turbulent boundary layer which forms within two coolant hole diameters of injection. As a result, the turbulent jet decreases adiabatic effectiveness but does not have a substantial effect on the heat transfer coefficient. The span-wise averaged adiabatic effectiveness agrees well with experiments for a turbulent coolant jet, without which the calculated effectiveness is over-predicted. On the other hand, the heat transfer coefficient which is only a function of near wall turbulence, shows good agreement with experiments for both coolant jet inlet conditions.
© 2007 Elsevier Inc. All rights reserved.

Keywords: Large eddy simulation; Leading edge film cooling; Adiabatic effectiveness; Heat transfer coefficient

1. Introduction

The overall thermal efficiency of gas turbine engines can be effectively improved by increasing the turbine inlet temperature. However, these high operative temperatures affect the durability of the blade. To prevent damage to the blades, a variety of cooling techniques have been developed. These techniques fall into two major categories; internal and external cooling. Both techniques use cold air extracted from the compressor section and pass it through channels within the blade (internal cooling), where tabulators such as ribs and pin fins are used to increase the rate of heat removal. The cooling air then is ejected into the mainstream through holes located on the leading edge, suction and pressure sides of the blade to provide a thin cold film of air which prevents the direct contact of hot gases with the blade surface (film cooling) [Han (2004)]. Although cooling techniques increase the durability of the engine, the reduction in the operative fluid mass flow rate due to the air extraction from the compressor section is detrimental to the overall performance. This has led to numerous studies to determine factors which impact blade cooling in an attempt to optimize the process.

A considerable portion of these investigations are specific to leading edge film cooling. Due to the exposure to a high heat load, prediction of the flow field in this region is important and essential to blade durability. On the other hand, the complexity of the flow field and geometry makes

---

* Corresponding author. Tel.: +1 540 231 9975; fax: +1 540 231 9100.
  E-mail address: dtafti@vt.edu (D.K. Tafti).

Nomenclature

BR	blowing ratio (u_c/u_∞)	x	physical coordinates
C_s	Smagorinsky constant	θ	non-dimensional temperature ($\theta = (T - T_c)/(T_\infty - T_c)$)
D	leading edge diameter		
d	coolant hole diameter	ζ	computational coordinates
H	channel height	δ	boundary layer thickness in stagnation region
k	thermal conductivity	υ	kinematic viscosity
L	coolant hole length to diameter ratio	τ	non-dimensional time
n	normal wall distance		
Nu	Nusselt number ($Nu = hD/k$)	*Subscripts*	
Pr	Prandtl number ($Pr = \nu/\alpha$)	aw	adiabatic wall
P	Span-wise pitch to hole diameter ratio	b	bulk
q''	heat flux	c	coolant
R	temporal autocorrelation	t	turbulent parameters
Re	Reynolds number ($Re = u_\infty D/\nu$)	τ	values based on friction velocity
S	strain rate tensor	∞	free stream
S	arc length along cylinder surface		
T	temperature	*Superscripts*	
u	cartesian velocity vector/stream-wise velocity	*	dimensional parameter
U	contravariant velocity vector		

it complicated and difficult to study. Therefore, for the sake of simplification, many studies on the leading edge film cooling have represented the leading edge with a blunt body and a semi-cylindrical leading edge. Of the experimental studies, one can mention an early study by Mick and Mayle (1988), followed by a study of Mehendale and Han (1992), and studies by Salcudean et al. (1994), Ekkad et al. (1998), Ou and Rivir (2001), and Ekkad et al. (2004). A common conclusion from these studies is that increasing the mainstream turbulence is detrimental to film cooling effectiveness, but the negative effect is minimized at high coolant-mainstream blowing ratios. Heat transfer coefficient is not sensitive to mainstream turbulence but is affected significantly by coolant-mainstream blowing ratio. Adiabatic effectiveness is sensitive to the geometry and arrangement of the cooling holes, but overall, it decreases at high blowing ratios due to higher dispersion of the coolant and entrainment of mainstream gas between the coolant jet and blade surface due to lift off. The experimental studies of Cruse (1997), Yuki et al. (1998), and Johnston et al. (1999) used a half-section of a blunt body with quarter of a cylindrical leading edge. A suction channel was located below the stagnation line to stabilize and fix the stagnation line in its location. This experimental setup has been used to validate several numerical studies. Chernobrovkin and Lakshminarayana (1999) simulated this geometry utilizing a number of low Reynolds number k–ε models for turbulence closure. The results were in good agreement with experimental data. They identified four major vortices and explained their origins and their effects on effectiveness. Shyy et al. (1999) simulated the jets and free-stream interaction around a low Reynolds number airfoil leading edge. The SIMPLE algorithm was used with a

k–ε model with a low Reynolds number treatment to model the turbulence. The boundary condition at the hole exit was adopted from a previous study done by Thakur et al. (1999). Lin and Shih (2001) used Menter's k–ω shear stress transport (SST). The results were in reasonable agreement with experimental data. They identified the formation of separation bubbles caused by the hole–plenum interaction and horseshoe vortices which caused the hot gas entrainment. York and Leylek (2002a,b) used a realizable k–ε model in the Fluent code. Local and laterally averaged film cooling effectiveness was predicted but numerical results showed over-prediction in the region between the stagnation line and second row of holes when compared to the experimental data. They speculated that this discrepancy could be due to the unsteadiness about stagnation in the experiment, which was not taken into account. They also predicted the heat transfer coefficient which showed good agreement with experimental data at low blowing ratios.

In another study by Azzi and Lakehal (2001), two classes of k–ε model and Reynolds stress transport model were used to simulate both a flat plate and a symmetrical turbine blade. In the first case, a two-layer approach was used where a DNS-based one-equation model was applied in the viscous region and k–ε model was applied in the outer region. It was found that the isotropic two-layer model under-predicted the lateral temperature distribution and resulted in lower effectiveness compared to the experimental data. To account for anisotropy effects, a factor was introduced with the eddy viscosity in the near wall one-equation model. In the second case, various quadratic and cubic explicit algebraic stress models combined with the DNS-based near wall region one-equation model were used. While the non-linear algebraic model provided some-

what better results, the best results were obtained from the two-layer method with anisotropic DNS-based one-equation model in the near wall region. However, they suggested that this method needed a more refined mesh near the walls. Theodoridis et al. (2001) used a standard k–ε model with wall function to simulate a turbine blade film cooling without lateral injection. Turbulence intensity predicted in the stagnation region was not realistic. Turbulence anisotropy was found to be much less on the suction side compared to the pressure side. Applying the anisotropy correction of Bergeles et al. (1978) resulted in a much better prediction of temperature on the pressure side.

2. Objective of the study

The literature review reveals that RANS models are partially successful in simulating film cooling. Eddy viscosity models under-predict the lateral spreading of the temperature field and the discrepancies with the experimental data increase at high blowing ratios. In leading edge film-cooling the additional physical complexity introduced by flow stagnation, free-stream turbulence, pressure gradients and flow acceleration, and boundary layer transition further limit the capability of RANS models as effective prediction tools. Optimizing film cooling requires a more fundamental understanding of the phenomenon which can only be obtained by quantifying the time-dependent dynamic characteristics of flow and heat transfer. Large eddy simulation (LES) is capable of providing such data. The advantages of LES over RANS simulations are many, not the least among them, the elimination of the empiricism of RANS models. In spite of the need for this capability, a few studies such as Tyagi and Acharya (2003), Lui and Pletcher (2005), Iourokina and Lele (2005, 2006), and Guo et al. (2006) have been conducted with LES for film cooling on a flat plate. In spite of being computationally challenging, the flat plate geometry alleviates a lot of the geometrical/meshing requirements and ensuing numerical complexities associated with leading edge film cooling. The objective of the proposed study is to push the state-of-the-art in the application of LES by extending it to leading edge film cooling to elucidate on the unsteady flow physics and heat transfer. This study investigates the effect of the coolant pipe inlet boundary condition on mixing and the resulting adiabatic effectiveness and heat transfer coefficient.

3. Solution methodology

3.1. Computational model and the governing equations

The governing flow and energy equations are non-dimensionalized by a characteristic length scale which is the leading edge diameter of the cylinder (D^*), a characteristic velocity scale given by the inlet free-stream velocity (u_∞^*). Two characteristic temperature scales are incorporated: ($T_\infty^* - T_c^*$) in calculating the adiabatic effectiveness

and $\frac{q_w'' D^*}{k}$ in calculating the heat transfer coefficient. The time-dependent Navier–Stokes and energy equations are non-dimensionalized in transformed coordinates (Thompson et al., 1985) as:

Continuity:

$$\frac{\partial}{\partial \xi_j}(\sqrt{g}\overline{U^j}) = 0 \tag{1}$$

Momentum:

$$\frac{\partial}{\partial t}(\sqrt{g}\bar{u}_i) + \frac{\partial}{\partial \xi_j}(\sqrt{g}\overline{U^j}\bar{u}_i) = -\frac{\partial}{\partial \xi_j}(\sqrt{g}(\vec{a}^j)_i\bar{p})$$
$$+ \frac{\partial}{\partial \xi_j}\left(\left(\frac{1}{Re} + \frac{1}{Re_t}\right)\sqrt{g}g^{jk}\frac{\partial \bar{u}_i}{\partial \xi_k}\right) \tag{2}$$

Energy:

$$\frac{\partial}{\partial t}(\sqrt{g}\bar{\theta}) + \frac{\partial}{\partial \xi_j}(\sqrt{g}\overline{U^j}\bar{\theta}) = \frac{\partial}{\partial \xi_j}\left(\left(\frac{1}{PrRe} + \frac{1}{Pr_tRe_t}\right)\sqrt{g}g^{jk}\frac{\partial \bar{\theta}}{\partial \xi_k}\right) \tag{3}$$

where $\vec{a}^i$ are the contravariant basis vectors[1], $\sqrt{g}$ is the Jacobian of the transformation, g^{ij} is the contravariant metric tensor, $\sqrt{g}U^j = \sqrt{g}(\vec{a}^j)_i u_i$ is the contravariant flux vector, u_i is the Cartesian velocity vector, and θ is the non-dimensional temperature.

The overbar in the continuity, momentum and energy equations denote grid filtered quantities. Re_t is the inverse of the non-dimensional turbulent eddy-viscosity and is obtained by the Smagorinsky model

$$\frac{1}{Re_t} = C_s^2(\sqrt{g})^{2/3}|\bar{S}| \tag{4}$$

where $|\bar{S}|$ is the magnitude of the strain rate tensor given by $|\bar{S}| = \sqrt{2\overline{S_{ik}S_{ik}}}$. The Smagorinsky constant C_s^2 is obtained via the dynamic procedure [Germano et al. (1991)]. The turbulent Prandtl number is assumed to have a constant value of 0.5 [Moin et al. (1991)].

3.2. Numerical method

The governing equations for momentum and energy are discretized with a conservative finite-volume formulation using a second-order central difference scheme on a non-staggered grid topology. The Cartesian velocities, pressure, and temperature are calculated and stored at the cell center, whereas, contravariant fluxes are stored and calculated at the cell faces. A projection method is used for time integration. The temporal advancement is performed in two steps, a predictor step, which calculates an intermediate velocity field, and a corrector step, which calculates the updated velocity at the new time step by satisfying discrete continuity.

---

[1] The notation $(\vec{a}^j)_i$ is used to denote the ith component of vector $\vec{a}^j$, $(\vec{a}^j)_i = \partial\xi_j/\partial x_i$.

The computer program GenIDLEST (Generalized Incompressible Direct and Large-Eddy Simulations of Turbulence) used for these simulations has been applied extensively to study flow and heat transfer in stationary and rotating internal ducts, heat exchangers, etc. [Abdel-Wahab and Tafti (2004), Sewall and Tafti (2006, 2007), Sewall et al. (2006), Cui and Tafti (2002), Tafti and Cui (2003)]. Details about the algorithm, functionality, and capabilities of GenIDLEST can be found in Tafti (2001).

3.3. Experimental and computational geometries

The geometry is adopted from the experimental setup of Ekkad et al. (1998), where a cylinder (with a tailboard placed at the rear) represents the leading edge. Two rows of cooling holes are located $\pm 15°$ from the stagnation line, each containing ten holes. The holes are at $30°$ and $90°$ inclination with span-wise and stream-wise direction, respectively. Based on the characteristic length scale of cylinder diameter D^* (7.62 cm), the channel height $H^*/D^* = 10.0$, hole diameter $d^*/D^* = 0.063$, hole length to diameter ratio $L^*/d^* = 3.1$, and span-wise pitch to hole diameter ratio $P^*/d^* = 4.0$ specifies the computational geometry. Detailed specifics of the test model can be found in Ekkad et al. (1998).

In the current paper, two computational domains are used to represent this model. They are referred to as D-I and D-II from this point forward (see Fig. 1). D-I has the dimension of $10 \times 10 \times 0.252$ with the cylinder centered at (0,0,0). This domain has two rows of coolant holes on either side of stagnation. D-II is exactly half of the first domain, where a symmetry boundary condition is assumed along

the stagnation line. In both, the tailboard is replaced by a flat after body, to alleviate the unnecessary complications which arise due to flow separation in the wake of the cylinder. This change is not expected to adversely affect comparisons with experimental data in the near field of coolant injection.

3.4. Flow and boundary conditions

The mainstream Reynolds number is 100,000 based on the cylinder diameter and mainstream velocity. Coolant to mainstream density ratio is assumed to be unity, as in the experiment. In the current study a blowing ratio of $BR = 0.4$ is applied. The mainstream inlet condition is a constant velocity profile (u_∞) with no free-stream turbulence (experiments had a nominal $Tu = 0.5\%$) and a convective outflow condition is applied.

Two different coolant pipe inlet conditions are tested. First, a constant velocity profile (CVP) with a value of 0.4 at the coolant pipe inlet (which gives a blowing ratio of 0.4) in the direction of the coolant pipe axis is applied. Second, the coolant pipe inlet assumes a time-dependent turbulent velocity profile (TVP), which is obtained from an auxiliary fully developed turbulent pipe flow LES. The simulation results with CVP are used for comparison between domains D-I and D-II. Afterwards, both pipe inlet conditions are applied to domain D-II to study their effects on the film cooling phenomenon.

On the outer channel walls, wall boundary conditions with zero heat flux are assumed. In calculating the adiabatic effectiveness, an adiabatic condition is imposed on the blade surface. With non-dimensional temperature defined as $\theta = \dfrac{T^* - T_c^*}{T_\infty^* - T_c^*}$, the coolant and mainstream temperatures are denoted by 0 and 1, respectively. In calculating the heat transfer coefficient, a constant non-dimensional heat flux of unity is imposed on the cylinder surface and the mainstream and coolant temperatures – here non-dimensionalized with $\dfrac{q_w'' D^*}{k}$ – are set to zero. These selected conditions are consistent with the experimental conditions. As mentioned earlier, a symmetry boundary condition is imposed along the stagnation line for domain D-II.

In the current study, we choose not to place a plenum (which would be computationally simpler) in order to have greater control and definition over the jet inlet conditions, both in the mean flow distribution and turbulent characteristics. For the second set of calculations with a time-dependent turbulent inlet profile, it is implicitly assumed that the coolant hole is sufficiently long for the flow to exhibit a fully-developed turbulent flow at the location where the inlet boundary condition is applied.

3.5. Fully developed time-dependent turbulent coolant inlet boundary condition

Turbulent inflow conditions for the cooling pipe inlet uses scaled data from auxiliary simulations in a fully-devel-
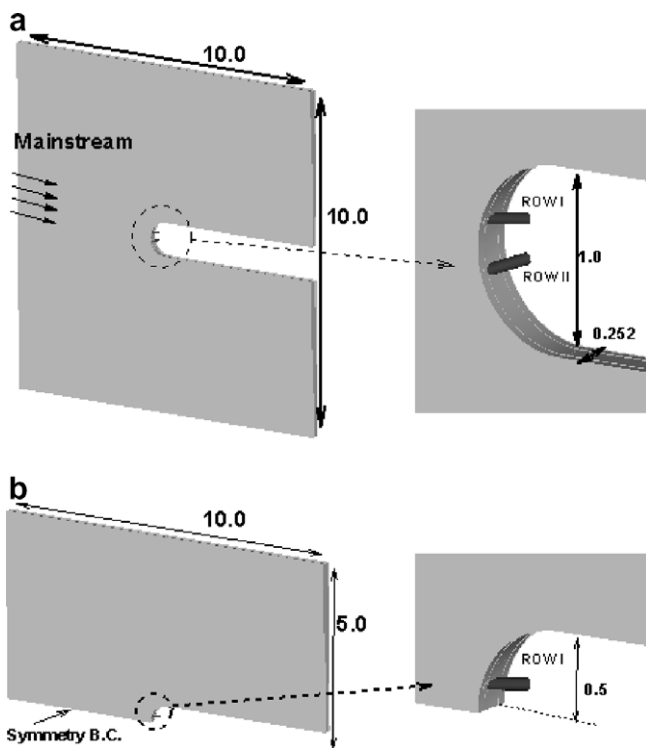

Fig. 1. Computational domains (a) D-I and (b) D-II.

oped pipe flow at an equivalent coolant jet Reynolds number. The auxiliary pipe flow simulations are carried out separately and validated with the experimental data of den Toonder and Nieuwstadt (1997). The pipe diameter is selected as the characteristic length scale and the pipe length is π. The grid consists of five blocks with a total resolution of $32 \times 32 \times 32 \times 5$ cells and has the same cross-sectional distribution and resolution as the coolant pipe, which provides 4–5 grid points in the distance of $y^+ = 10$ at the Reynolds number of 6200 based on pipe diameter and bulk velocity of the flow.

Fig. 2 shows the comparison of calculated and experimental stream-wise mean velocity and rms fluctuation plotted in wall-coordinates in a fully-developed pipe flow at a bulk Reynolds number of 6200 with available experimental data at 4900 and 10,000 (and also 17,800 for mean veloc-

ity). Agreement with the experimental data is good, in spite of a relative coarse grid used in the cross-section, which was limited by the permissible resolution in the main simulation. For further validation of the results' accuracy, the calculated friction coefficient was compared to the Petukhov correlation for fully developed flows [Petukhov (1970)] as:
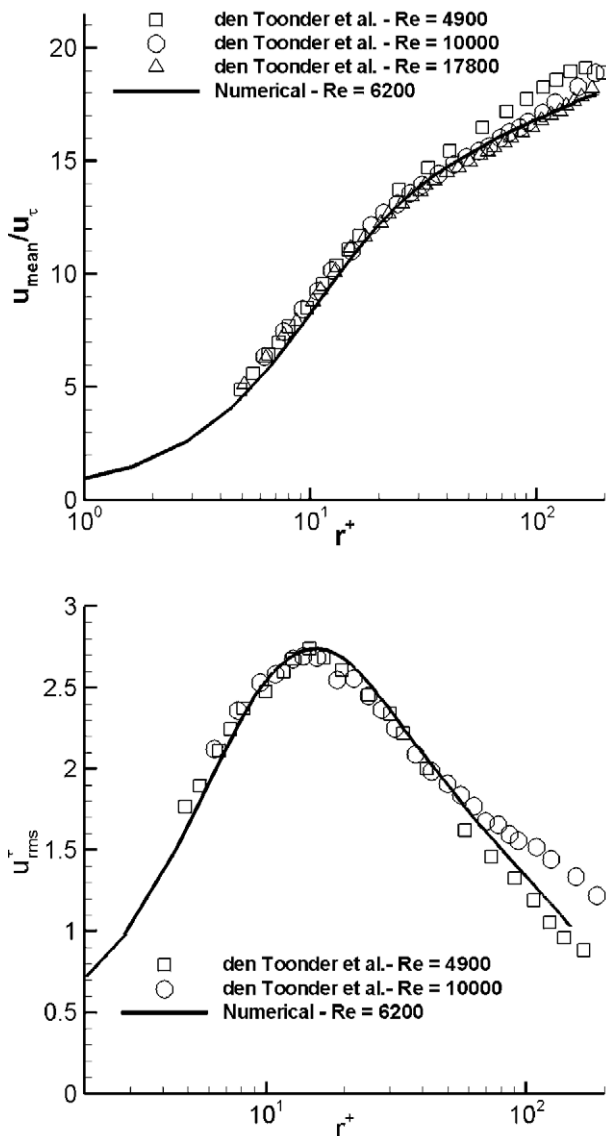
$$f = 0.25(0.790 \ln Re_D - 1.64)^{-2} \quad 3000 \leqslant Re_D \leqslant 5 \times 10^6$$
(5)

Results obtained from the simulation and correlation are 9.438×10^{-3} and 9.008×10^{-3}, respectively.

A finite number of stored time-dependent frames from this auxiliary calculation are cycled at the inlet plane of the coolant pipe in the main simulation. To calculate the suitable number of frames, autocorrelations for the three velocity components (u, v, and w) are evaluated at the center of the pipe. As shown in Fig. 3, the autocorrelation quickly falls to zero for all three velocity components within a non-dimensional time unit of 0.1. However, the turbulent signal in this time span does not give adequate resolution over a range of frequencies. Hence frames were stored for one non-dimensional time unit (50,000 frames) to represent the turbulence at the inlet to the coolant hole. The last 1000 frames act as a buffer and are modified such that the last frame of one cycle correlates with the first frame of the next cycle. This ensures a smooth transition between the two cycles.

Once the frames are calculated and stored, a transformation matrix is used to scale the velocity components according to the blowing ratio and align the resultant velocity vector with the coolant pipe axis. The scaling factor used is the velocity ratio between the coolant velocity and pipe flow mean velocity ($u_c/u_{\text{mean,pipe}}$). Fig. 4 shows the effect of the inlet conditions CVP and TVP on the mean profile of the axial velocity in the coolant jet and turbulent kinetic energy at the exit plane of the coolant pipe. It is noted that the outward flow to the surface is negative by virtue of its direction, hence, the positive velocities at the

Fig. 2. Mean profile and turbulent statistics in an auxiliary turbulent pipe flow simulation. Numerical results are compared to experimental data of den Toonder and Nieuwstadt (1997).
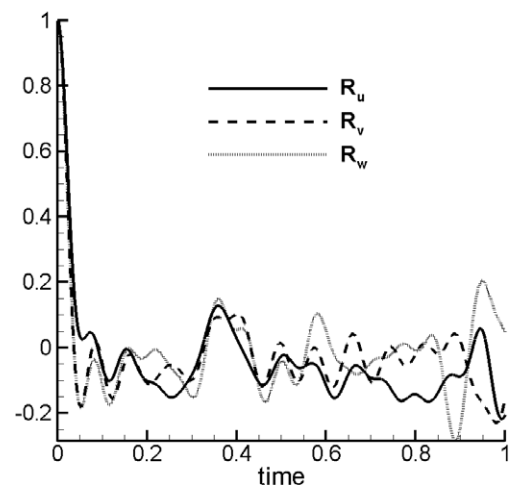

Fig. 3. Temporal autocorrelation for velocity components.
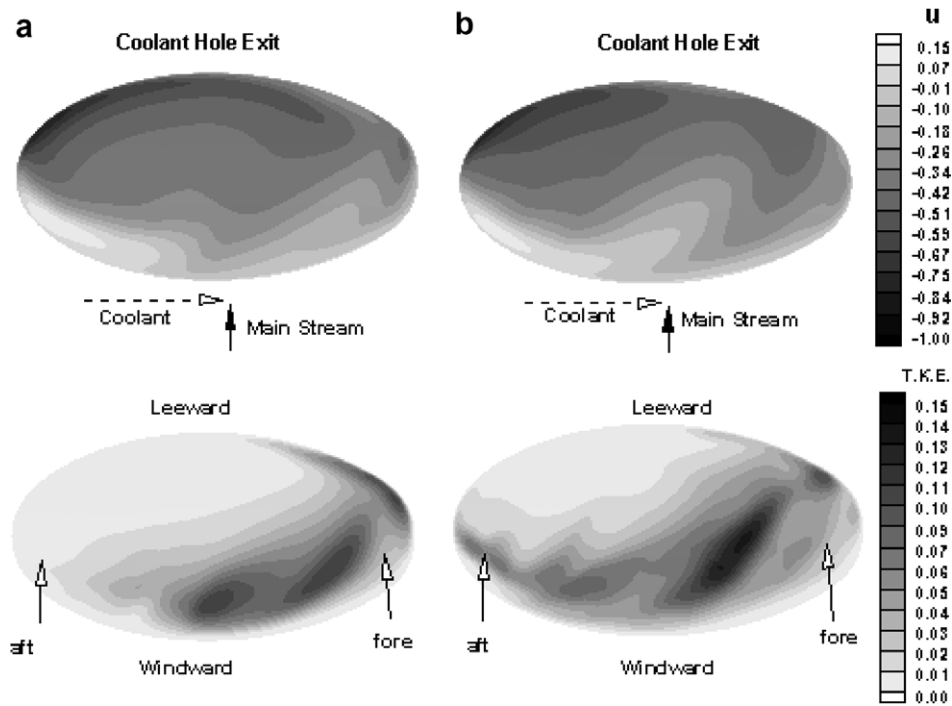
Fig. 4. Mean axial velocity and turbulent kinetic energy at exit plane of coolant pipe for (a) CVP and (b) TVP conditions.

windward side of the coolant hole indicate penetration of the mainstream flow into the coolant pipe, which is estimated to be about $0.3d$ for both cases. The infiltration of the mainstream into the coolant pipe pushes the coolant to the aft-leeward-side of the hole from which it ejects with a high velocity. The exit mean profiles between the two pipe inlet conditions are similar, except for some differences near the windward side.

The exit distribution of turbulent kinetic energy (T.K.E.) is noticeably different between the two cases. The T.K.E. at the exit is higher in case of TVP than it is for CVP. The maximum T.K.E. increases up to 15% for TVP with higher values in the rest of the exit plane, versus 10% for the CVP condition.

3.6. Grid properties

The complex geometry at the leading edge needs to be meshed with a high quality grid, with minimal skewness and discontinuities in grid size to maintain a good quality solution and prevent numerical instabilities from developing during time integration. A factor which has a large influence on the grid generation process is the large variation in turbulent length scales between the coolant and external flow. Based on an external Reynolds number of 100,000, $d^*/D^* = 0.063$, and a blowing ratio of 0.4, the viscous length scale associated with near wall turbulence in the cooling jet is of $O(1 \times 10^{-3}d^*)$, whereas, the external geometrical length scale is of $O(D^*)$, both of which have to be reconciled in the grid generation process.

The complex leading edge geometry is meshed by using a multiblock framework. While each block has a structured body-fitted mesh, an unstructured block topology is utilized. This method provides the flexibility of unstructured meshes with the good physical and computational properties of structured meshes. A multi-block grid, generated with Gridgen 15.07, consists of 124 blocks with 6,422,528 cells for domain D-I and 62 blocks with 3,211,264 cells for domain D-II. A non-conformal interface approach is used to relax the grid requirements far from the cylinder surface.

The grid resolution is tested *a-posteriori* by using the calculated local shear stress to find $y^+ = yu_\tau/v$. The distribution of y^+ shows that the condition of $y_1^+ < 1$ is satisfied on the entire cylinder surface. Results also show that approximately 45 grid points lie within the boundary of coolant–mainstream interaction downstream of the coolant hole [Rozati and Tafti (2007)]. It is noteworthy that the resolution and grid spacing for domain D-II is identical with the upper half of domain D-I. Therefore, the justifying arguments on grid resolution for domain D-I are perfectly applicable for the second domain (D-II) as well.

4. Results and discussion

The calculation was carried out on Virginia Tech's Terascale computing facility, SystemX, on 2.3 GHz PowerPC 970 FX processors (124 and 62 processors for domains D-I and D-II, respectively). The non-dimensional time step was set to 3×10^{-5} and 2×10^{-5} for CVP and TVP conditions, respectively. Each time step took approximately 4.5 s of wall clock time. The flow is allowed to develop for approximately three time units before sampling and averaging to obtain mean quantities is activated. Probes

at various locations in the jet and downstream of injection are monitored to estimate the time evolution of the flow.

4.1. Stagnation line dynamics

During the course of the computations with domain D-I, it was found that the stagnation line did not remain stationary at the center but moved for both coolant inlet conditions. Fig. 5 shows the time evolution of the stagnation line for the two cases studied. The motion of the stagnation line is more gradual with the CVP condition than with the TVP condition, which is consistent with the fact that the TVP at the coolant inlet introduces more asymmetries into the calculation because of the turbulent nature of the jet. It is noted that the physical time during which this happens is less than 27 ms from startup, and could be a transient with the stagnation line returning to its location at steady state. The other possibility which cannot be discounted is that the stagnation line oscillates even after steady state is reached. In either case, to resolve this motion, which is on a much longer time scale than the turbulent time scale of jet–mainstream interaction (and is of primary interest in this study), would be prohibitively expensive.

Many experimental studies have used a modified geometry, which only includes one-half of the cylindrical leading edge with a suction slot to bleed-off the boundary layer and control the location of the stagnation line [Cruse (1997), Yuki et al. (1998), and Johnston et al. (1999)]. In doing this, an implicit assumption made is that the behavior of the coolant–mainstream interaction pertinent to the adiabatic effectiveness and heat transfer coefficient on one side

is unaffected by the dynamics on the other side. The same tact is followed in this study by assuming symmetry along the stagnation line (domain D-II).

To validate this assumption, the cross-correlation between the flow field generated by the two jets is studied to assure that elimination of the bottom coolant row does not affect the characteristics of the top coolant row. Fig. 6 shows the locations at which the flow is monitored. All points shown in Fig. 6 are located at the jet centerline plane ($z = 0$) and distributed downstream of the coolant hole as follows: P-1 and P-5 at $s/d = 0$, P-2 and P-6 at $s/d = 1.25$, P-3 and P-7 at $s/d = 2.22$, P-4 and P-8 at $s/d = 3.75$, and P-9 at $s/d = 6.1$. In domain D-I, the same distribution of monitored points lies downstream of the bottom coolant hole. While some of the points lie in the near wall region inside the turbulent boundary layer that develops after injection, others lie at the outer boundary of coolant–mainstream interaction. The cross-correlation is calculated from: $R = \dfrac{\overline{u_1' u_2'}}{u_{\mathrm{rms1}} u_{\mathrm{rms2}}}$, where 1, and 2 correspond to the top and bottom half of the cylinder, respectively.

Table 1 shows the values of cross-correlation between the velocity components. Considering the full spectrum of results obtained over all the points, we can draw the conclusion that the generated turbulent fields have a very weak correlation between the two sides. Therefore, in the current study, a symmetric boundary condition along the stagnation line is imposed as described by domain D-II. The imposition of the symmetry boundary is further validated *a-posteriori* by comparing some key mean results obtained in D-II with D-I with the CVP coolant inlet condition.
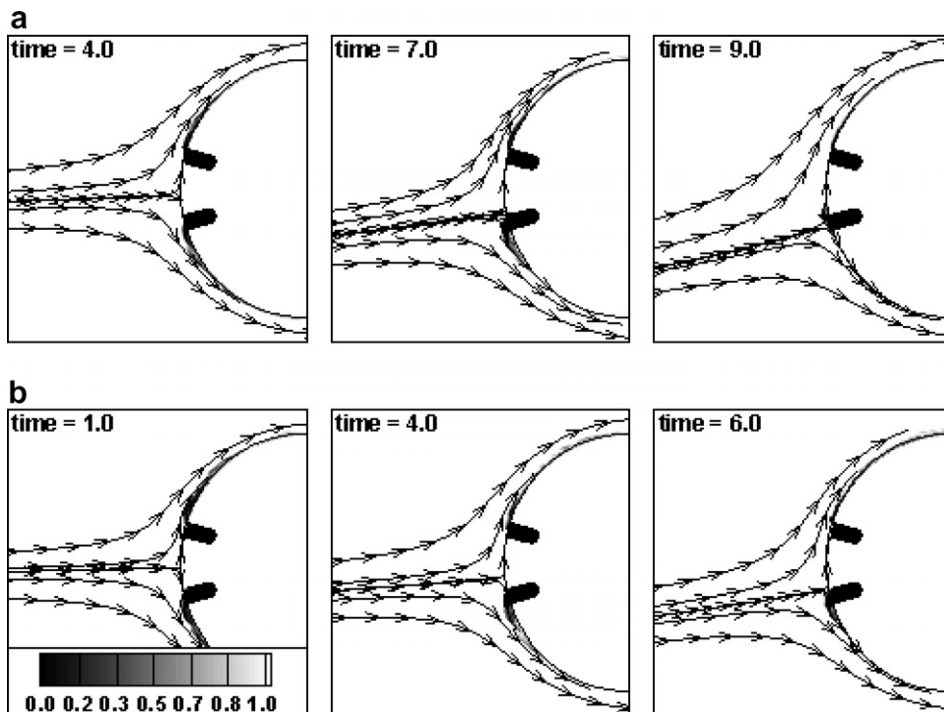

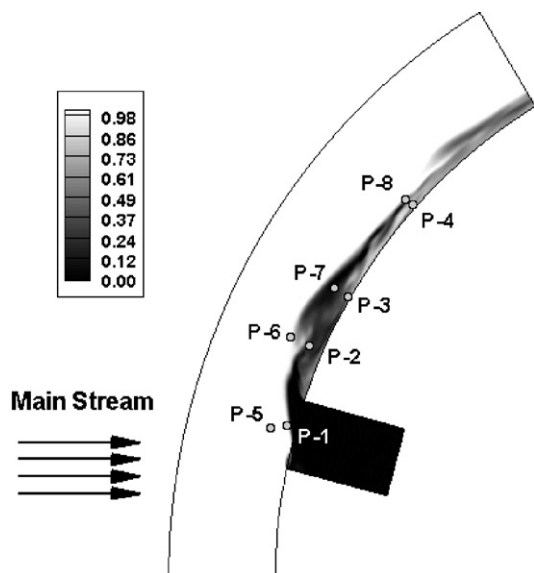Fig. 5. Unsteadiness of stagnation line with (a) CVP and (b) TVP conditions.

Fig. 6. Location of the monitored points downstream of the coolant hole. Temperature contours are shown.

Table 1
Cross correlation between the two halves of domain D-I

Probe number	Cross correlation of u fluctuation	Cross correlation of v fluctuation	Cross correlation of w fluctuation
1	0.1077	0.0430	0.0901
2	−0.1537	0.0604	−0.0684
3	0.0113	0.2338	0.0617
6	−0.0013	0.2009	0.2401
7	−0.0351	−0.1030	−0.0267
8	0.0673	−0.1506	0.0506

Comparisons of mean temperature and velocity profiles, adiabatic effectiveness and turbulent quantities validate that domain D-II is a good approximation to D-I.

4.2. Turbulent flow features

The signal characteristics between D-I and D-II for CVP are compared at three selected locations (P-1, 4, and 8) in Fig. 7. This figure shows the turbulent characteristics in the flow downstream of the coolant hole by presenting the stream-wise velocity fluctuations. Probes are placed near the surface to resolve the developing turbulent boundary layer and at the outer boundary of the shear layer resulting from the coolant–mainstream interaction (see Fig. 6 for locations). Qualitatively, the signals exhibit the same unsteady characteristics between the two domains. The effect of the unsteady stagnation line is observed in domain D-I at P-1 and P-8 which is located in the jet–mainstream shear layer away from the surface. At time $t = 4$, the stagnation line starts to move towards the bottom coolant hole row, resulting in additional acceleration of the stream-wise velocity on the top section of the leading edge.

Flow development is also analyzed by study the stream-wise velocity fluctuations downstream of injection. At the hole center, P-1 characterizes the jet–mainstream interac-
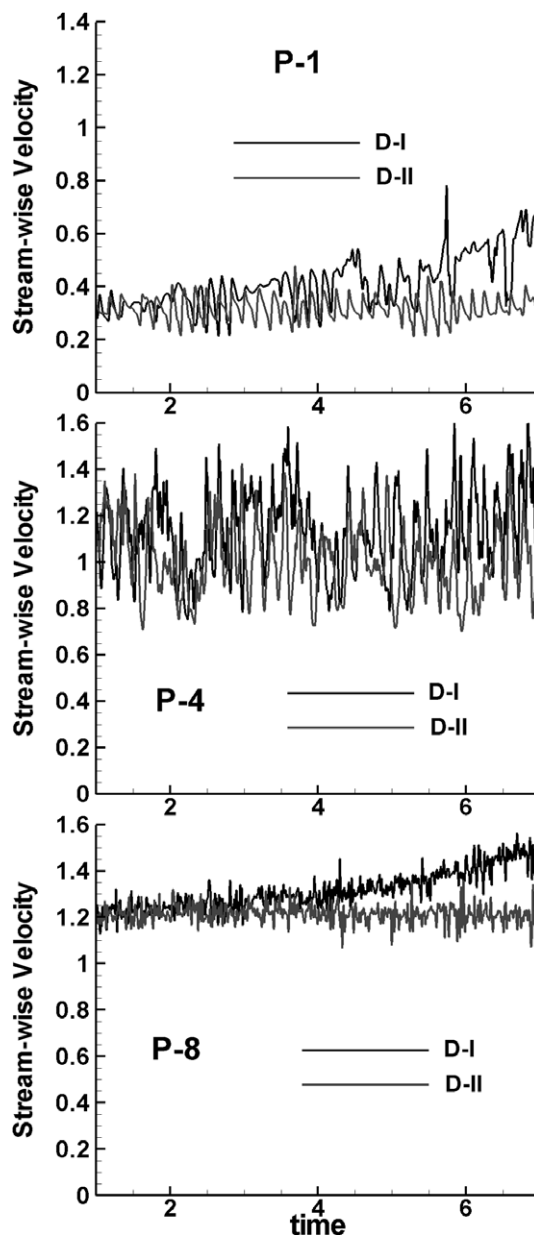

Fig. 7. Comparison of time history of stream-wise velocity for selected probes.

tion. As the coolant reaches 1.25 hole diameter downstream (P-2) from the hole center, the flow exhibits a strong turbulent behavior near the surface, which signals the development of a turbulent boundary layer. As the flow moves further downstream, the stream-wise velocity accelerates and the intensity of the fluctuations decreases for P-3 and P-4 compared to P-2. Farther from the surface, one can observe the development of a turbulent shear layer between the coolant and mainstream (P-5, 6, 7, and 8).

Power spectral density (PSD) comparisons between CVP and TVP inlet conditions are made at points P-2 and P-6 (Fig. 8). Point P-6, which lies in the outer shear layer between the jet and the mainstream, exhibits substantial difference in its turbulence content. While CVP has lesser turbulent content with energy concentrated in a few
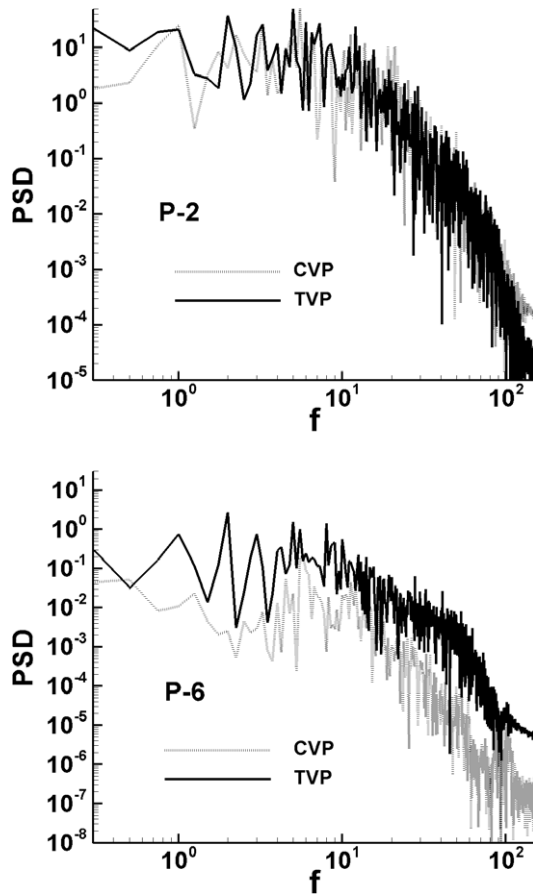
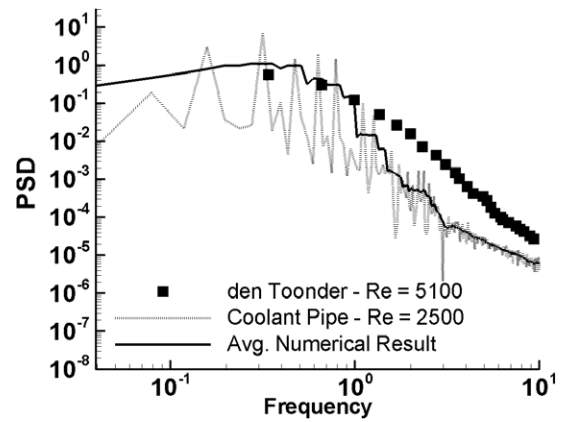Fig. 8. Power spectral densities of selected locations with CVP and TVP.

Fig. 9. PSD of axial coolant velocity at $0.5D$ from exit at $y^+ = 6$.

and pipe diameter to match the experiments. While the experimental location is at $y^+ \sim 12$, the approximate location in terms of y^+ in the coolant pipe is calculated to be 6. A number of low frequency peaks are observed in the spectrum, which are characteristic of the fundamental cycling frequency introduced at the pipe inlet. However, in spite of the energy being concentrated at select low frequencies, the energy distribution in the coolant jet is quite similar to the energy content in a fully-developed pipe flow. The similarity is more apparent when the experimental results are compared with the smoothed (averaged) numerical data[2].

4.3. Near wall coolant–mainstream mixing mechanism

The mixing mechanism of coolant and mainstream, coherent structures and their role in entrainment of hot gases underneath the coolant are similar for both domains, and for both boundary conditions at the coolant pipe inlet. To describe this process, the following definition is used to describe the location of flow/structures from this point forward: in the lateral direction, the side that the jet blows from is specified with prefix "aft" and the side the jet blows to, specified with prefix "fore". In the stream-wise direction along the blade surface, "leeward" is used to denote the downstream side of the jet and "windward" the upstream side of the jet. All distances are measured from the hole center. Fig. 4 shows the notation used.

The dominant coherent structures for a classical jet in cross flow are: counter-rotating vortex pair in the wake of the jet, horseshoe vortex on the windward side of the jet, and shear layer vortices [Tyagi and Acharya (2003), Iourokina and Lele (2005)]. To identify the coherent structures in the present study, the vortex eduction technique proposed by Chong et al. (1990) is used. In this method, in regions dominated by vortical motion the velocity gradient tensor exhibits two eigenvalues which are complex conjugate. The magnitude of the eigenvalue is indicative of the strength of the vortex. The structures identified by this

frequencies, TVP shows a much broader frequency content which is a result of the turbulence in the coolant jet. In general, it is observed that points which lie in the boundary layer near the surface are not affected greatly by the turbulence content of the coolant jets as exemplified by P-2, whereas, points which lie in the outer shear layer are influenced by the TVP inlet condition. From these observations, it can be expected that the turbulence in the coolant jets will have an impact on jet–mainstream mixing in the outer shear layer, but will not directly influence mixing near the surface, which is dominated by the near wall entrainment in the wake of the jet.

It is noted that at P-6 with the CVP inlet, spectral peaks are observed between non-dimensional frequencies (based on D and u_∞) of 5 to 6. This characteristic frequency is observed at all the monitoring locations. On application of the TVP condition, in addition to the same characteristic frequency, f, between 5 and 6, which now is not as dominant as with CVP, additional energetic modes are also observed at $f = 1, 2, 3$ in the outer shear layer. These frequencies are a result of the artificial cycling introduced for TVP at $f = 1$. To explore this aspect further, the PSD of the axial velocity in the coolant jet about $0.5D$ from its exit is compared to the experiments of den Toonder and Nieuwstadt (1997) (Fig. 9). The frequency in this case is non-dimensionalized by the coolant flow bulk velocity

---

[2] To obtain the averaged data, Savitzky–Golay filter from Matlab is used.

method are referred to as "coherent vorticity" in this paper, and the magnitude of the eigenvalue as the strength of the vortices.

Fig. 11 shows an instantaneous snapshot of coherent vorticity. An immediate observation is the complete absence of a horseshoe vortex. This is due to the combination of the low injection ratio and the compound angle injection. Pressure contours in planes normal to the surface and at the leeward-side of the hole at $s/d = 1.0$, show a low pressure region at the hole centerline (Fig. 10). This low pressure region is responsible for creating a strong counter-rotating vortex pair which entrains hot mainstream gases underneath the coolant jet. The primary structure forms immediately at the leeward edge of the hole (Fig. 11) and is transported downstream to form packets of hairpin vortices. This agrees with the observations of Tyagi and Acharya (2003) for a jet in cross flow in a flat plate boundary layer. However, as we can see in the pressure contours in Fig. 10, the strength of these counter-

rotating vortices is not equal, and the structure at the aft-side of the jet has considerably higher strength and size due to the lateral direction of coolant injection. Compared to a classical jet in cross flow, additional structures in the form of vortex tubes form at the windward side of the coolant hole. They are produced by the interaction of the transverse jet velocity and the mainstream flow. These vortex tubes bend towards the mainstream direction, on top of the hairpin vortices. It is noted that the vortex tubes are not stationary structures but constantly move fore-to-aft along the windward rim of the hole. Vortex tubes on the top of the jet break down quickly and assimilate with the vortex packet within 1–2 diameters downstream of the jet, while the structures at the aft- and fore-edge of the hole are stronger and directly participate in the jet–mainstream dynamics. One of these tubes is seen to extend at least $6d$ downstream of the jet, aiding the entrainment of hot gases.

Fig. 12 explains the jet–mainstream interaction mechanism by means of instantaneous temperature contours
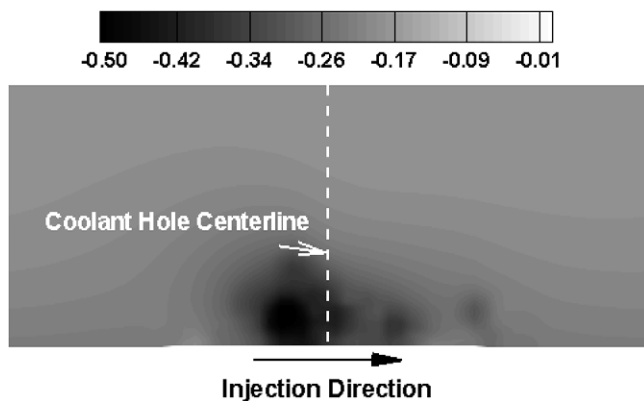

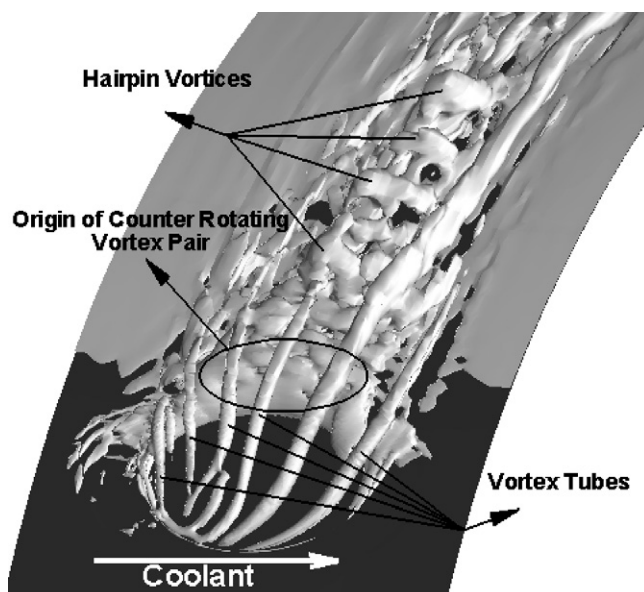Fig. 10. Pressure contour at $s/d = 1.0$ downstream of the coolant hole.
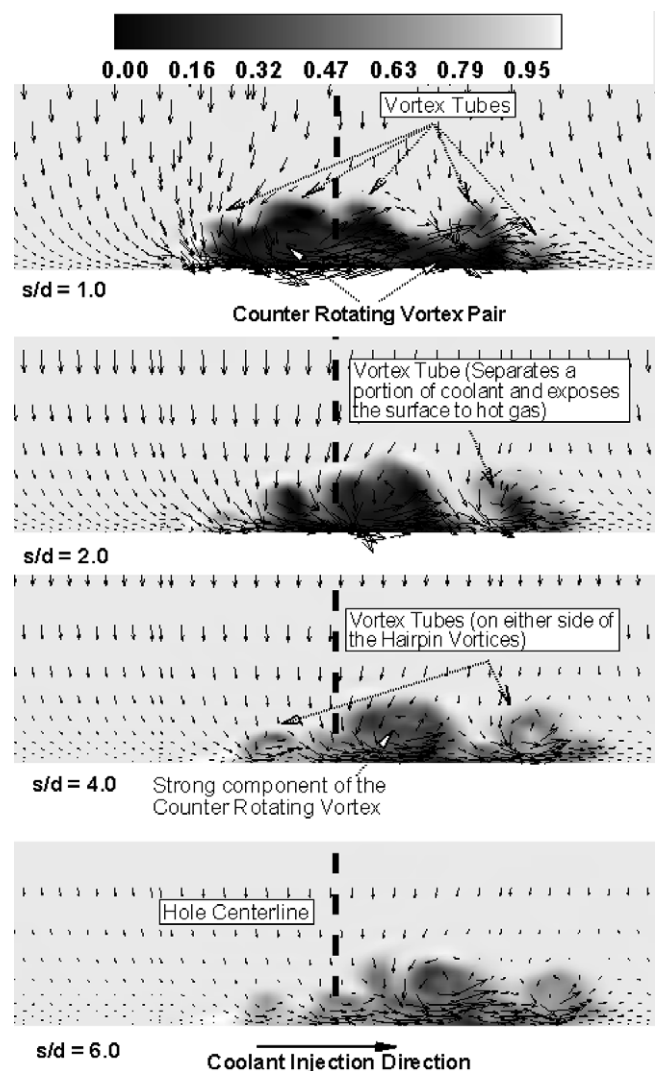

Fig. 11. Instantaneous coherent structures.

Fig. 12. Temperature contour and velocity vectors on cross-sectional planes normal to the surface and downstream the hole.

and velocity vectors in planes normal to the blade surface and downstream of the jet. At $s/d = 1.0$, one can identify vortex tubes on the top and sides of the counter-rotating vortex pair. The strength of the main counter-rotating vortex aided by the outer vortex tubes near the aft-side causes the bulk of the hot gas entrainment. As the jet travels downstream ($s/d = 2.0$), the strength of the primary counter-rotating vortex decreases. Eventually at $s/d = 4.0$, the weak component of the counter-rotating vortex pair, at the fore-side of the jet, disappears. As mentioned earlier, vortex tubes travel on the top and sides of the primary vortex structure. The tubes located at the top join with the stronger component of the counter-rotating vortex pair and contribute to entraining hot gas into the coolant from the aft-side. Vortex tubes located at the sides of the primary structure remain intact and separate. At $s/d = 2.0$, the vortex tube on the fore-edge of the coolant jet is seen to entrain hot gases. The side vortex tubes periodically cause the coolant flow to break off and join again with the main portion of the coolant jet. Due to the lateral velocity component of the coolant, it is observed that at $s/d = 6.0$ the jet completely shifts to the fore-side.

4.3.1. Mean profiles

Fig. 13 shows the mean velocity profiles of flow parallel to the surface of the cylinder at four locations downstream of the coolant hole and along its centerline. The profiles are plotted versus the normal distance from the surface normalized by the coolant pipe diameter. The velocity distribution at $s/d = 1.0$, in the immediate wake of the jet is characterized by a large velocity defect and the beginning of a boundary layer which results from lateral flow entrainment into this region. At this location, the maximum velocity at $0.325–0.35d$ from the surface is representative of the center of the coolant jet penetration into the mainstream and coincides with the location of minimum temperature (at jet centerline) in Fig. 14. By $s/d = 2.0$, a turbulent boundary layer is established as the mainstream flow accelerates. Interestingly, very minor differences are observed
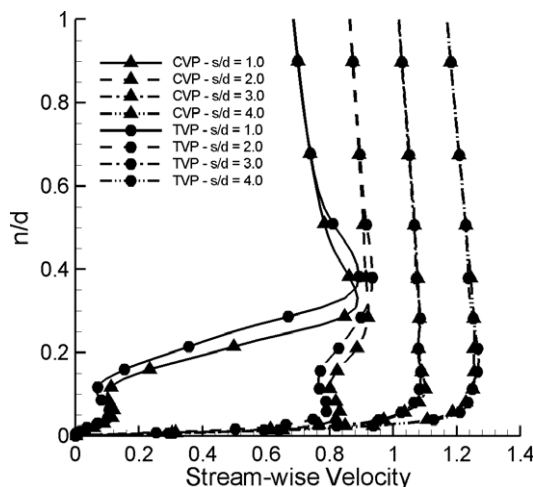

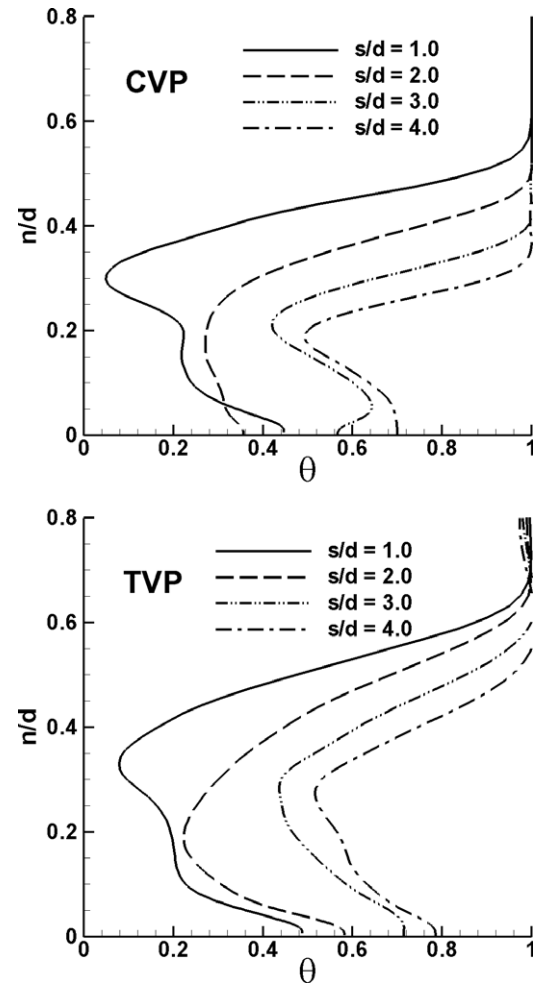Fig. 13. Mean velocity profiles parallel to the surface of the cylinder.

Fig. 14. Time-averaged temperature profile normal to the wall at jet centerline for CVP and TVP conditions.

between CVP and TVP, chief among them being the slightly larger penetration of the coolant jet with TVP.

Fig. 14 shows non-dimensional wall adiabatic temperature profiles at the centerline and downstream of the hole for the adiabatic effectiveness calculations. A high wall temperature in Fig. 14 implies lower effectiveness. At $s/d = 1.0$, for both inlet conditions, CVP and TVP, the wall temperature is approximately $0.45–0.5$. This confirms the strong unsteady hot gas entrainment underneath the coolant jet shown in Fig. 12 at $s/d = 1.0$ and confirmed by the mean velocity profile in Fig. 13. However, a notable difference between the two is the recovery of the wall temperature at $s/d = 2.0$. While for the CVP inlet, the wall temperature decreases, pointing to coolant diffusing into this region between $s/d = 1.0$ and $s/d = 2.0$, with the TVP condition, the recovery does not occur and the wall temperature increases monotonically with stream-wise distance. Another notable difference between the two coolant pipe inlet conditions is the extent of the thermal mixing layer. A thicker thermal layer is present with TVP indicating more mixing between the coolant and mainstream. The enhanced mixing can also be deduced from the profiles themselves, which are somewhat flatter with TVP. The increased mixing

with TVP is consistent with the earlier observation in Fig. 8 that the outer shear layer between the jet and the mainstream is more turbulent.

4.3.2. Turbulent statistics and kinetic energy

Turbulent kinetic energy behavior along the stream-wise direction is shown in Fig. 15, and Fig. 16 shows the rms distributions. The distributions are along the hole centerline, normal to the surface and are only shown at four locations, and as such, do not give a complete picture but only aid in identifying the major features of the turbulent field. At $s/d = 1.0$, two peaks appear in the T.K.E distribution, one very close to the surface and another between 0.1 and $0.2d$. The inner maximum close to the wall results from the strong lateral entrainment of fluid into the wake of the jet and is supported by the high values of w_{rms} at the same location. The outer maximum is a result of the interaction between the main body of the coolant jet with the mainstream. While this peak steadily decreases further downstream from the injection location as the coolant jet loses momentum, the inner peak increases up to $s/d = 2.0$ and then settles down to a near constant value, typical of turbulent boundary layers between 0.015 and 0.02 U_∞^2. A noticeable difference between CVP and TVP is observed in the T.K.E profiles in the outer part or in the region of jet–mainstream interaction. At all locations, TVP exhibits higher values of T.K.E. For example, at $s/d = 2.0$ and $n/d = 0.2$, the respective T.K.E. values are 0.018 versus 0.008 for TVP and CVP, respectively. This trend is present at all streamwise locations and the differences are particularly evident in the outer part of the jet–mainstream interaction zone. These observations are consistent with earlier observations made in Figs. 8 and 14.

Turbulent statistics show maximum rms values at $0.2d$ from the surface in the region of coolant–mainstream interaction at the centerline ($z/D = 0.0$) and $s/d = 1.0$ for u_{rms} and v_{rms}[3]. However, w_{rms} exhibits two peaks, representative of the jet–mainstream interaction and the turbulence generated by the lateral entrainment of hot gases in the near wall region. Further downstream, as in the T.K.E. profiles, the maximum rms values shift to the near wall region, where a turbulent boundary layer is developing. In the near wall region at $s/d = 1.0$, the turbulence exhibits strong anisotropy. While u_{rms} and v_{rms} values show somewhat similar values and profiles, w_{rms} shows a very different distribution and higher magnitude, due to the strong lateral entrainment. As the coolant travels downstream, the stress components become more isotropic in the outer part. As was observed in the T.K.E. profile, the rms values are higher farther from the wall with TVP condition and downstream of the coolant hole compared to the results with CVP condition.

T.K.E. contours in the span-wise direction also give useful information on the effect of inlet turbulence on the effectiveness in Fig. 17. The three locations correspond to the aft edge ($z/D = -0.015$), center ($z/D = 0.0$) and fore-side ($z/D = 0.015$) of the coolant hole. The contours show that the maximum values of T.K.E. occur at the leeward and aft-side of the coolant hole. The jet–mainstream interaction shear layer thickness is thicker and more elongated with the TVP condition. Also, the T.K.E. contained in the aft vortex tube and on the top center of the coolant hole have higher values with TVP condition. The higher T.K.E on the aft-side of the coolant jet results in more entrainment of mainstream fluid which results in lower adiabatic effectiveness distribution and narrower coverage. Conversely, on the fore-side, the CVP condition results in higher T.K.E. values in the vortex tube.

4.3.3. Adiabatic effectiveness

Adiabatic effectiveness is used to quantify the attachment of the coolant to the blade surface given by:

$$\eta = \frac{T_{aw}^* - T_\infty^*}{T_c^* - T_\infty^*} \quad \text{or} \quad \eta = 1 - \theta_{aw} \qquad (6)$$

Fig. 18 compares the distribution of adiabatic effectiveness with TVP and CVP inlet conditions. At the low blowing ratio studied, the adjacent holes in the span-wise
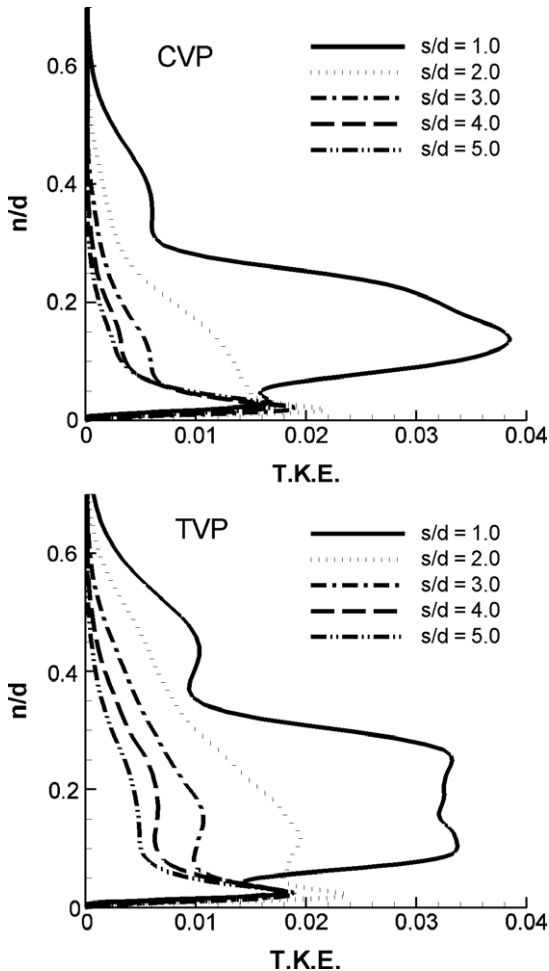

Fig. 15. T.K.E profile along stream-wise for CVP and TVP conditions.

---

[3] The directions of u_{rms} and v_{rms} coincide with the flow direction and the direction normal to flow, respectively, and not with the x- and y-axes.
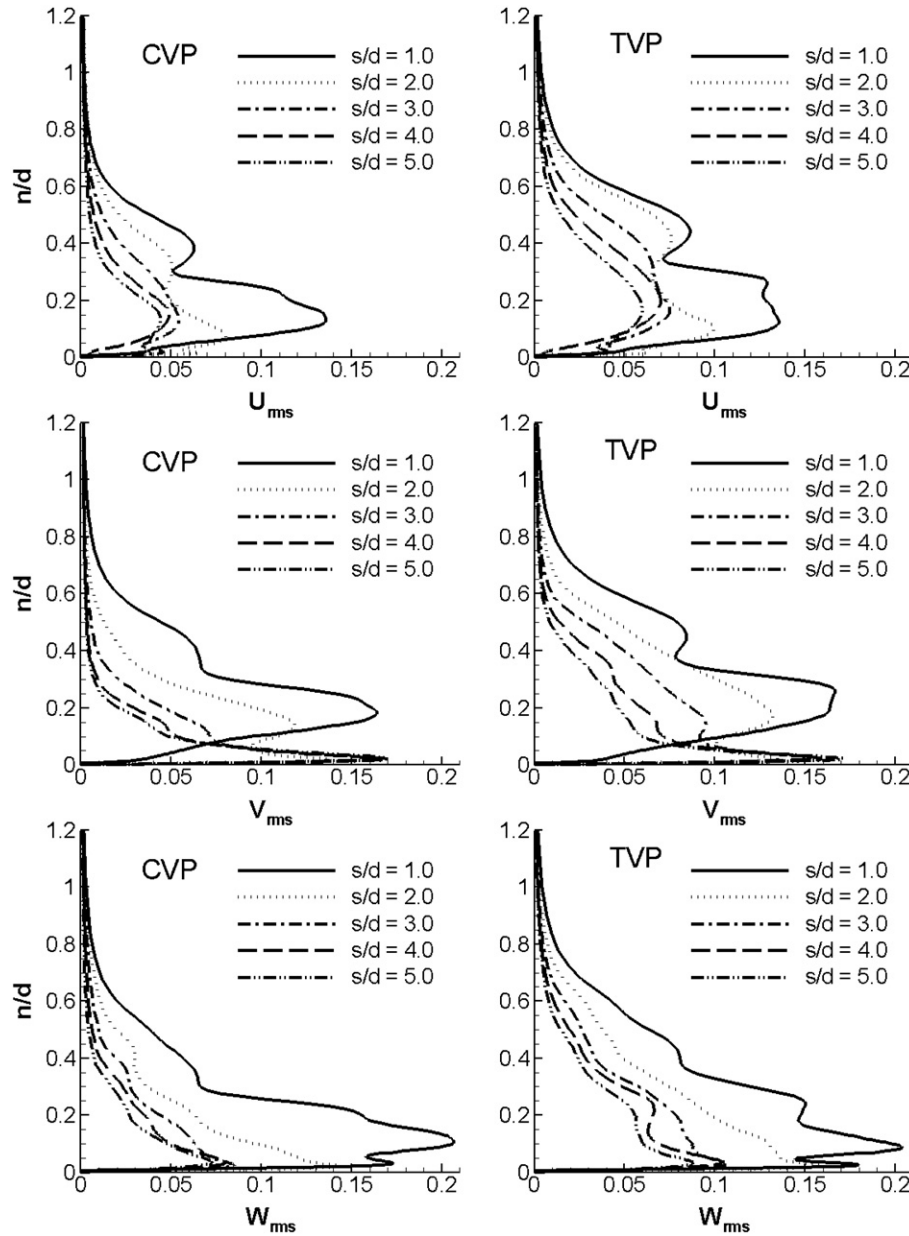
Fig. 16. Turbulent statistics' profile along stream-wise direction for CVP and TVP conditions.

direction have no effect on each other and the coolant does not provide good coverage to the full pitch, but is washed down with the strong mainstream flow for both coolant pipe inlet conditions. In the near field immediately downstream of coolant ejection, the TVP condition results in lower effectiveness at the fore-lee side of the jet because of increased mixing with the turbulent jet. Another observed difference is the narrower spread of the jet on the leeside as it diffuses downstream with the TVP condition. A quantitative comparison with Ekkad et al. (1998) is made in Fig. 19 which plots the span-wise averaged adiabatic effectiveness downstream of coolant injection. As observed earlier, the CVP condition calculates a higher adiabatic effectiveness than TVP, whereas, the TVP inlet coolant condition compares very favorably with the

experiments. While the experimental jet inlet conditions are not documented, it is our expectation that the coolant issuing from the exit will be turbulent due to the sharp shear layers which usually form at the entrance to the coolant pipe from the plenum.

4.3.4. Heat transfer coefficient

The heat transfer coefficient is expressed in terms of the Frossling number, $Nu/Re^{1/2}$. Based on the non-dimensionalization used, the Nusselt number is calculated as

$$Nu_i = \frac{1}{\theta_w - \theta_{ref}} \tag{7}$$

where θ_w is the wall temperature subjected to a non-dimensional heat flux of unity, and θ_{ref} is the reference tempera-
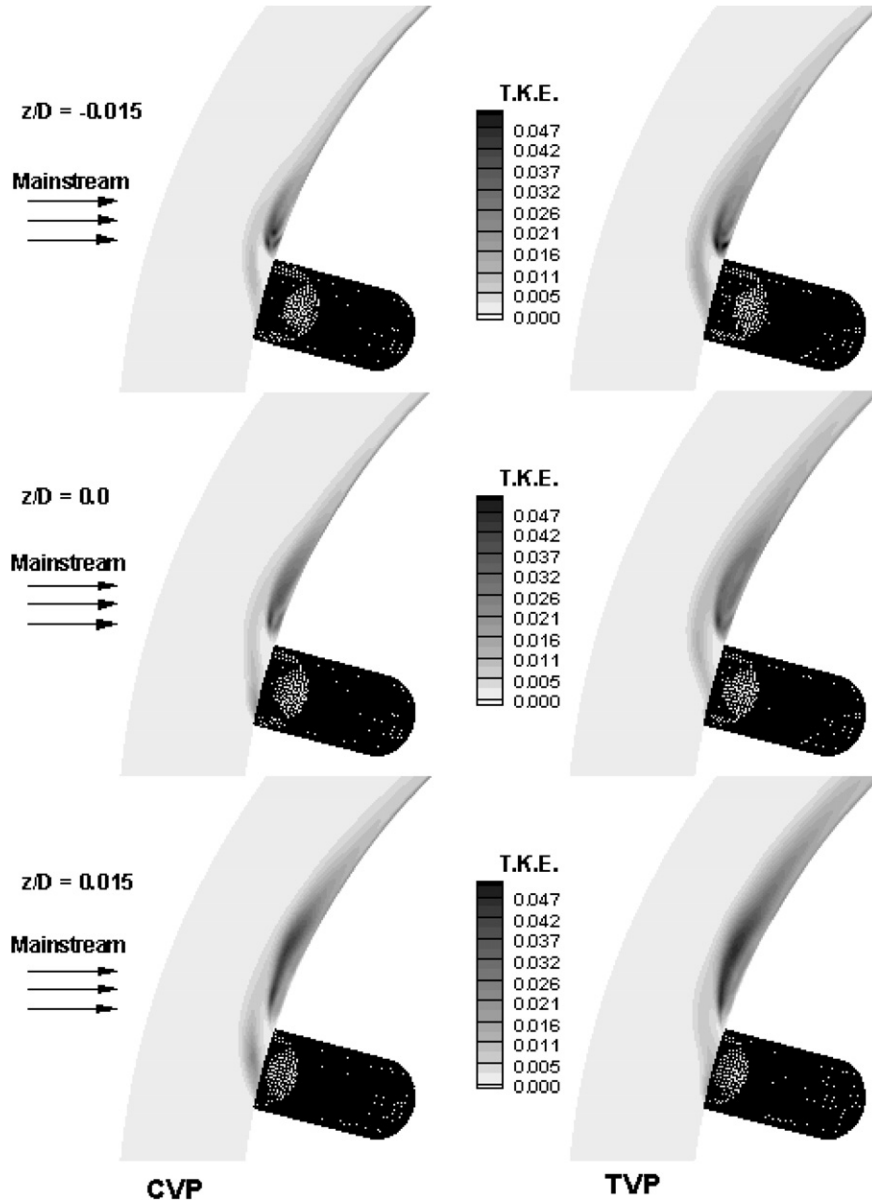
Fig. 17. T.K.E. contours in span-wise direction for CVP and TVP conditions.

ture equal to the mainstream bulk temperature ($\theta_{ref} = 0.0$). Fig. 20 shows the surface distribution of Frossling number for the two coolant pipe inlet conditions CVP and TVP. Unlike the large differences in adiabatic effectiveness, minor differences exist between the two, which at first seems counter intuitive. However, as noted earlier in the distribution of turbulence, the TVP condition mostly affects turbulence in the outer layer and not so much near the wall. Hence, its effect on lowering adiabatic effectiveness comes from enhanced mixing between the coolant and the mainstream away from the surface which increases the adiabatic wall temperature. On the other hand, the heat transfer coefficient is strongly dependent on turbulence in the near wall region, which does not change substantially between the two cases (see Figs. 15 and 16). The conclusions reached are very similar to the effect of free-stream turbu-

lence, which at low blowing ratios decreases the adiabatic effectiveness but has a small effect on heat transfer coefficients [Ekkad et al. (1998)].

Three regions of high heat transfer coefficients located at the aft- and fore-side of the coolant hole are observed, all of which can be directly related to near wall coherent structures. Fig. 21 shows the mean structures identified by taking the time mean of the instantaneous coherent vorticity magnitudes. The mean structures identified in the figure manifest the persistent instantaneous coherent vorticity. The region of high heat transfer which begins at the aft edge of the jet and which shifts towards the centerline of the hole in Fig. 20 results from the entrainment dynamics of the stronger component of the counter-rotating vortex pair, which is represented by the blob of coherent vorticity immediately downstream of injection. The regions of high heat
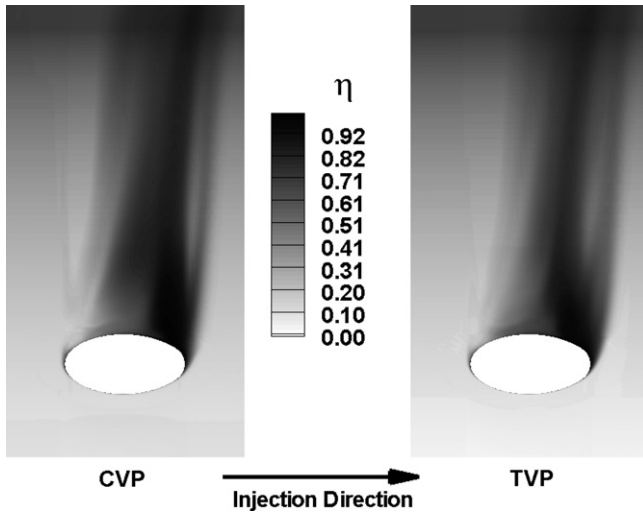
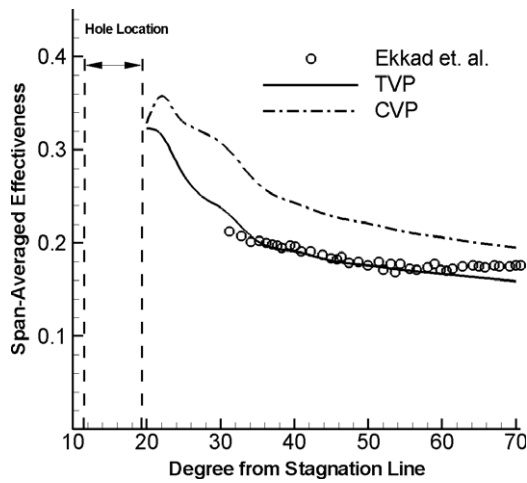Fig. 18. Surface distribution of adiabatic effectiveness for CVP and TVP conditions.
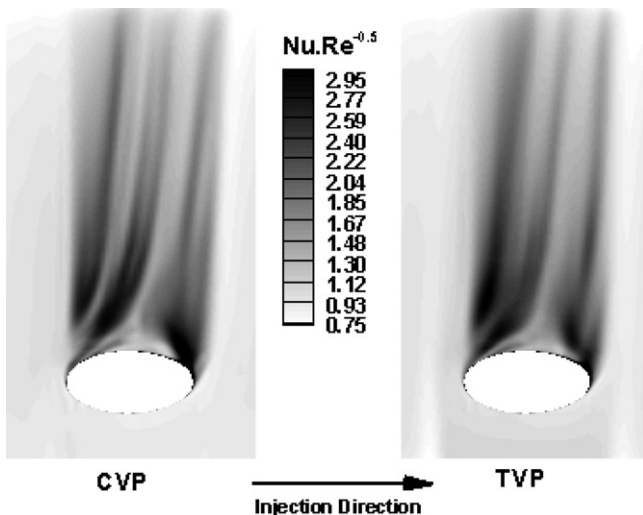

Fig. 21. Effect of mean coherent structures on heat transfer coefficient.

Fig. 19. Span-wise averaged adiabatic effectiveness distribution.
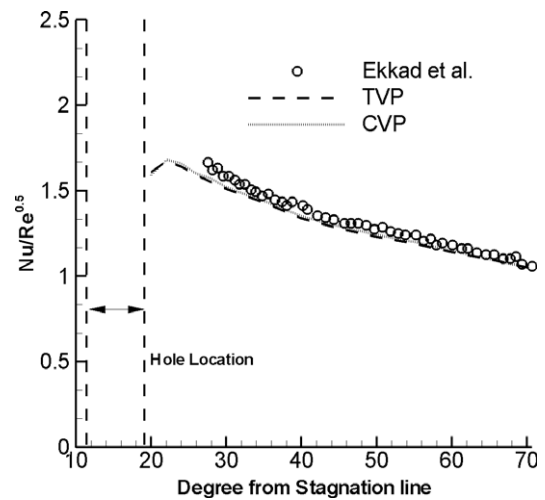
Fig. 22. Span-wise averaged Frossling number distribution.

Fig. 20. Surface Frossling contours for CVP and TVP conditions.

transfer coefficients at the fore and aft edges of the holes are a direct result of the instantaneous vortex tubes which are shown at these locations in Figs. 11 and 12. These structures are temporally persistent and have a strong identity in the mean and their proximity to the wall produces strong temperature gradients. A quantitative comparison is obtained with the span-wise-averaged Frossling numbers in Fig. 22, which show excellent agreement.

5. Summary and conclusions

A representative leading edge film cooling geometry has been modeled with large eddy simulation to analyze the coolant–mainstream flow interaction at a free-stream Reynolds number of 100,000 and a blowing ratio of 0.4. Two rows of compound angle injection holes are located ±15° from stagnation. The calculation (i) investigated the effect

of coolant pipe inlet condition on film cooling effectiveness and heat transfer coefficient, (ii) identified the important coherent structures and their effect on adiabatic effectiveness and the heat transfer coefficient, (iii) described the coolant mixing process with the mainstream and main flow entrainment, and (iv) provided turbulent statistics and detailed adiabatic effectiveness and heat transfer coefficient distributions.

The results show the existence of an asymmetric counter-rotating vortex pair in the immediate wake of the coolant jet. The driving mechanism for the formation of these vortices is a low pressure zone in the wake which entrains mainstream flow laterally into this region. The vortex on the fore-side of the jet is much weaker and quickly loses its identity within $s/d = 2.0$ downstream of the injection. In addition to these primary structures, the lateral injection of the coolant and its interaction with the mainstream flow result in the formation of tube vortices on the windward side of the coolant hole which are convected downstream over and to the aft- and fore-side of the counter-rotating vortex pair. While some of the vortex tubes merge with the counter-rotating vortex pair quickly, others located aft and fore of the jet maintain a separate identity and play a dominant role in the entrainment of hot gases and in augmenting the heat transfer coefficient.

Two coolant pipe inlet conditions are studied: a constant velocity profile at the inlet with no turbulence, and a turbulent profile. In the former, in spite of the absence of turbulence in the mainstream and the jet, the jet–mainstream interaction results in the flow becoming turbulent immediately downstream of the jet with the formation of a turbulent boundary layer. A characteristic low frequency interaction between the jet and the mainstream is clearly identified at a non-dimensional frequency (based on D and u_∞) between 5 and 6. On introducing turbulence in the coolant jet, mixing with the mainstream in the outer region of the jet is increased. However, the jet turbulence does not directly impact near wall turbulence which is dominated by three-dimensional entrainment in the wake of the jet. As a result, adiabatic effectiveness decreases due to greater mixing between the jet and the mainstream, whereas, the heat transfer coefficient is not affected significantly.

The comparison of span-wise averaged adiabatic effectiveness and Frossling number showed excellent agreement with experimental data. Surface distributions of adiabatic effectiveness show that the coolant does not provide full coverage in the span-wise direction at the low blowing ratio studied. Surface distributions of time-averaged Frossling number show that regions of high heat transfer coefficients can directly be related to coherent structures in the immediate wake of the jet.

References

Abdel-Wahab, S., Tafti, D.K., 2004. Large eddy simulations of flow and heat transfer in a 90° ribbed duct with rotation – effect of coriolis and centrifugal buoyancy forces. Journal of Turbomachinery 126, 627–636.

Azzi, A., Lakehal, D., 2001. Perspective in modeling film cooling of turbine blades by transcending conventional two-equation turbulence model. In: Proceedings of IMECE'01, November 11–16, 2001, New York, NY.

Bergeles, G., Gosman, A.D., Launder, B.E., 1978. The turbulent jet in a cross stream at low injection rates: A three-dimensional numerical treatment. Numerical Heat Transfer 1, 217–242.

Chernobrovkin, A., Lakshminarayana, B., 1999. Numerical simulation and aerothermal physics of leading edge film cooling. Proceedings of Institution of Mechanical Engineers 213-A, 03–118.

Chong, M.S., Perry, A.E., Cantwell, B.J., 1990. A general classification of three dimensional flow fields. Physics of Fluids A 2 (5), 765–777.

Cruse, M.W., 1997. A study of film cooling adiabatic effectiveness for turbine blade leading edges. M.S. Thesis, The University of Texas, Austin, Texas.

Cui, J., Tafti, D.K., 2002. Computations of flow and heat transfer in a three-dimensional multilouvered geometry. International Journal of Heat and Mass Transfer 45 (25), 5007–5023.

den Toonder, J.M.J., Nieuwstadt, F.T.M., 1997. Reynolds number effects in a turbulent pipe flow for low to moderate Re. Journal of Physics of Fluids 9 (11), 3398–3409.

Ekkad, S.V., Han, J.C., Du, H., 1998. Detailed film cooling measurement on a cylindrical leading edge model: Effect of free-stream turbulence and coolant density. Journal of Turbomachinery 120, 799–807.

Ekkad, S.V., Ou, S., Rivir, R.B., 2004. A transient infrared thermography method for simultaneous film cooling effectiveness and heat transfer coefficient measurements from a single test. Journal of Turbomachinery 126, 597–603.

Germano, M., Piomelli, U., Moin, P., Cabot, W.H., 1991. A dynamic subgrid-scale eddy viscosity model. Physics of Fluids 3, 1760–1765.

Guo, X., Schroder, W., Meinke, M., 2006. Large-eddy simulation of film cooling flows. Computers and Fluids, 587–6066.

Han, J.G., 2004. Recent studies in turbine blade cooling. International Journal of Rotating Machinery 10 (6), 443–457.

Iourokina, I.V., Lele, S.K., 2005. Towards large eddy simulation of film cooling flows on a model turbine blade leading edge. In: Forty-third AIAA Aerospace Science Meeting and Exhibit, 10–13 January 2005, Reno, Nevada.

Iourokina, I.V., Lele, S.K., 2006. Large eddy simulation of film cooling above the flat surface with a large plenum and short exit holes. In: Forty-fourth Aerospace Science Meeting and Exhibit, Jan 9–12 2006, Reno, NV.

Johnston, C.A., Bogard, D.G., McWaters, M.A., 1999. Highly turbulent mainstream effects on filmcooling of a simulated airfoil leading edge. ASME Paper No. 99-GT-261.

Lin, Y.L., Shih, T.I.P., 2001. Film cooling of a cylindrical leading edge with injection through rows of compound angle holes. Journal of Heat Transfer 123, 645–654.

Lui, K., Pletcher, R.H., 2005. Large eddy simulation of discrete-hole film cooling in a flat plate turbulent boundary layer. In: Thirty-eighth AIAA Thermophysics Conference, 6–9 June 2005, Toronto, Ontario, Canada, AIAA, 2005–4944.

Mehendale, A.B., Han, J.C., 1992. Influence of high mainstream turbulence on leading edge film cooling heat transfer. Journal of Turbomachinery 114, 707–715.

Mick, W.J., Mayle, R.E., 1988. Stagnation film cooling and heat transfer including its effect within the hole pattern. Journal of Turbomachinery 110, 66–72.

Moin, P., Squires, K., Cabot, W., Lee, S., 1991. A dynamic sub-grid-scale model for compressible turbulence and scalar transport. Physics of Fluids A 12, 2746–2757.

Ou, S., Rivir, R.B., 2001. Leading edge film cooling heat transfer with high free stream turbulence using a transient liquid crystal image method. International Journal of Heat and Fluid Flow 22, 523–614.

Petukhov, B.S., 1970. In: Irvine, T.F., Hartnett, J.B. (Eds.), Advances in Heat Transfer, vol. 6. Academic Press, New York.

Rozati, A., Tafti, D.K., 2007. Large eddy simulation of leading edge film cooling part-I: Computational domain and effect of coolant inlet

condition, ASME Paper No. GT2007-27689. In: Proceedings ASME Turbo Expo 2007: Power for Land, Sea and Air, May 14–17, 2007, Montreal, Canada.

Salcudean, M., Gartshore, I., Zhang, K., McLean, I., 1994. An experimental study of filmcooling effectiveness near the leading edge of a turbine blade. Journal of Turbomachinery 116, 71–79.

Sewall, E.A., Tafti, D.K., 2006. Large eddy simulation of flow and heat transfer in the 180° bend region of a stationary ribed gas turbine blade internal cooling duct. Journal of Turbomachinery 128, 763–771.

Sewall, E.A., Tafti, D.K., 2007. Large eddy simulation of flow and heat transfer in the developing flow region of a rotating gas turbine blade internal cooling duct with coriolis and buoyancy forces. Journal of Turbomachinery, in press.

Sewall, E.A., Tafti, D.K., Graham, A.B., Thole, K.A., 2006. Experimental validation of large eddy simulation of flow and heat transfer in a stationary ribbed duct. International Journal of Heat and Fluid Flow 27, 243–258.

Shyy, W., He, X., Thakur, S., 1999. Jets and free stream interaction around a low-Reynolds number airfoil leading edge. Numerical Heat Transfer, Part A 35, 891–902.

Tafti, D.K., Cui, J., 2003. Fin-tube junction effect on flow and heat transfer in flat tube multilouvered heat exchangers. International Journal of Heat and Mass Transfer 46, 2027–2038.

Tafti, D.K., 2001. GenIDLEST – A scalable parallel computational tool for simulating complex turbulent flowsProc. ASME Fluids Engineering Division, FED, vol. 256. ASME-IMECE, New York.

Thakur, S., Wright, J., Shyy, W., 1999. Convective film cooling over a representative turbine blade leading edge. International Journal of Mass Transfer 42, 2269–2285.

Theodoridis, G.S., Lakehal, D., Rodi, W., 2001. Three-dimensional calculations of the flow field around the turbine blade with film cooling injection near the leading edge. Flow, Turbulence and Combustion 66, 57–83.

Thompson, J.F., Warsi, Z.U.A., Mastin, C.W., 1985. Numerical Grid Generation Foundation and Applications. Elsevier Science Publishing Co., Inc., New York 10017.

Tyagi, M., Acharya, S., 2003. Large eddy simulation of film cooling flow from an inclined cylindrical jet. Journal of Turbomachinery 125, 734–742.

York, D.W., Leylek, J.H., 2002a. Leading edge film cooling physics: Part I – adiabatic effectiveness. In: Proceedings of ASME Turbo Expo 2002, June 3–6, 2002, Amsterdam, The Netherlands, ASME Paper No. GT-2002-30166.

York, D.W., Leylek, J.H., 2002b. Leading edge film cooling physics: Part I – adiabatic effectiveness. In: Proceedings of ASME Turbo Expo 2002, June 3–6, 2002, Amsterdam, The Netherlands, ASME Paper No. GT-2002-30167.

Yuki, U.M., Bogard, D.G., Cutbirth, J.M., 1998. Effect of coolant injection on heat transfer for a simulated turbine airfoil leading edge. ASME Paper No. 98-GT-431.